Angle-dependent magnetoresistance and quantum oscillations in high-mobility semimetal LuPtBi

To cite this article before publication: Xu et al, 2017, J. Phys.: Condens. Matter, at press:
https://doi.org/10.1088/1361-648X/aa6695

Angle-dependent magnetoresistance and quantum oscillations in high-mobility semimetal LuPtBi

Guizhou Xu[1,2] Zhipeng Hou[2], Yue Wang[2], Xiaoming Zhang[2], Hongwei Zhang[2], EnKe Liu[2], Xuekui Xi[2], Feng Xu[1], Guangheng Wu[2], Xi-xiang Zhang[3,*] and Wenhong Wang[2,†]

[1] Nanjing University of Science and Technology, School of Materials Science and Engineering, Nanjing 210094, China

[2] Institute of Physics, State Key Laboratory for Magnetism, Beijing National Laboratory for Condensed Matter Physics, Chinese Academy of Sciences, Beijing 100190, China

[3] King Abdullah University of Science and Technology (KAUST), Physical Science and Engineering, Thuwal 23955-6900, Saudi Arabia.

Email: xixiang.zhang@kaust.edu.sa or wenhong.wang@iphy.ac.cn.

Keywords: large magnetoresistance, quantum oscillations, LuPtBi, Fermi surface

Abstract

The recent discovery of ultrahigh mobility and large positive magnetoresistance in topologically non-trivial Half-Heusler semimetal LuPtBi provides a unique playground for studying exotic physics and significant perspective for device applications. As an fcc-structured electron-hole-compensated semimetal, LuPtBi theoretically exhibits six symmetrically arranged anisotropic electron Fermi pockets and two nearly-spherical hole pockets, offering the opportunity to explore the physics of Fermi surface with a simple angle-related magnetotransport properties. In this work, through the angle-dependent transverse magnetoresistance measurements, in combination with high-field SdH quantum oscillations, we achieved to map out a Fermi surface with six anisotropic pockets in the high-temperature and low-field regime, and furthermore, identify a possible magnetic field driven Fermi surface change at lower temperatures. Reasons account for the Fermi surface change in LuPtBi are discussed in terms of the field-induced electron evacuation due to Landau quantization.

1. Introduction

Semimetals have attracted increasing attention in physics and materials science in the past few years because of their fascinating physical phenomena arising from the unique Fermi-surface (FS) topology, which opens exciting opportunities to design new materials with novel properties [1-3]. In the large family of semimetallic systems, electron-hole compensated semimetals, such as bismuth [1,4], WTe_2 [2,5], $NbSb_2$ [3], and some heavy half-Heusler compounds [6-9], in contrast to the specific-band semimetals (such as Cd_3As_2 [10-12] and Na_3Bi [13] with Dirac nodes in their bulk FS), possess a near balance of the tiny electron and hole pockets, which is very sensitive to the external field. Therefore, the application of an external field can drastically affect their multi-physical quantities and induce interesting physical responses, such as valley-nematic Fermi liquid behavior for bismuth in magnetic field [14], dome-shaped superconductivity for WTe_2 under pressure [15,16]. In addition, many reports have revealed that magnetic field is able to alter electronic structure of the compensated semimetals and result in new field-induced physical properties, such as the large non-saturated positive magnetoresistance (MR) effect [2-5,8], which can be potentially applied in future spintronic devices.

As a strong spin-orbit coupling (SOC) system, heavy half-Heusler semimetals with nontrivial band inversion has been recently reported to exhibit many exotic physical phenomena, such as heavy fermions, non-centrosymmetric superconductors, and possible topological ordering behavior [17-21]. Among those, semimetal LuPtBi with the strongest SOC has attracted much attention. For example, recent ARPES studies [22,23] have confirmed the existence of the predicted topological surface states in LuPtBi, although they largely overlap with the bulk valence bands. Moreover, magneto-transport studies on LuPtBi reveal very large field-induced MR and ultrahigh carrier mobilities [8,9]. Interestingly, the temperature dependence of Hall resistivity and thermopower in LuPtBi are found to present abnormal sign reversal at high magnetic fields [8]. Such a sign reversal is reminiscent of the FS change (field-induced Lifshitz transition [24]) observed in some gapless semiconductors [25,26], which may be responsible for the observed large field-induced positive MR. In order to map the FS topology of LuPtBi, in this work, we employed the angle-dependent transverse MR, an effective probe method of highly symmetric bulk FS. In combination with the angular Shubnikov-de Haas quantum oscillations, we further indentified a possible field-induced FS change at low temperatures that shows

a less anisotropic near-ellipsoidal sphere Fermi pocket at high fields. We discussed the gradual loss of six-fold rotational symmetry of FS in terms of the field-induced band gap opening due to electron evacuation in the presence of Landau quantization.

2. Methods

Single crystals of LuPtBi were synthesized by a Bi self-flux method. The high-purity starting materials Lu (ingot, 99.99%), Pt (ingot, 99.99%) and Bi (ingot, 99.99%) were mixed together in a molar ratio of 1:1:10, and afterward the mixture was placed in an alumina crucible. This process was performed in a glove box filled with argon (Ar) gas, where the oxygen and humidity content was less than 0.5 ppm. The whole assembly was sealed inside a tantalum (Ta) tube under Ar gas. Then, the Ta tube was sealed into an evacuated quartz tube. The crystal growth was carried out in a furnace by heating the tube from room temperature up to 1150℃ over a period of 15h, holding at this temperature for 24h, and then slowly cooling to 650℃ at a rate of 2℃/h. The excess Bi flux was removed by spinning the tube in a centrifuge at 650℃. After the centrifugation process, most of the flux contamination was removed from the surfaces of crystals and the remaining topical flux was etched by diluted hydrochloric acid. The sizes of crystals were typically 1.5×1.2×0.8 mm^3; the crystals have mirror-like surfaces and robust in the air.

The composition of the single crystal samples was determined by energy-dispersive X-ray (EDX) spectroscopy which was equipped on a Hitachi S-4800 scanning electron microscope (SEM). The EDX measurements were performed at different positions on a crystal surface within instrument accuracy of 1-2%.The crystal structure of the single crystal was checked by powder x-ray diffraction (XRD) measurement which was carried out on crushed single crystals using a Rigaku X-ray diffractometer with Cu-$K\alpha$ radiation. The single-crystal orientation was checked by a standard Laue diffraction technique.

To measure the transverse MR, the four-probe methods were applied. The electrical leads were attached onto the polished crystals (~ 2.0×0.6×0.2 mm^3) in the long direction using silver paste by platinum wires, as seen in figure 1e. The angular

MR were obtained by rotating the sample to the field. The transport measurements were performed on a Quantum Design physical properties measurement system (PPMS), where the temperature can vary from 2 to 300 K.

The electronic structure calculations in this work were performed using full-potential linearized augmented plane-wave method, as implemented in the package WIEN2k. The exchange correlation of electrons was treated within the local spin density approximation (LSDA). Meanwhile, a 50×50×50 *k*-point grid was used in the calculations, equivalent to 125000 *k* points in the first Brillouin zone. Moreover, the muffin-tin radii of the atoms are 2.5 a. u., which are generated by the system automatically. The lattice parameters and atomic positions were taken from our experimental data. Fermi surface was visualized with XCrySden [27] using the same number of *k* points.

3. Calculated Fermi-surface and measurement setup.

As the magnetotransport properties of half-Heusler single crystals are strongly dependent on the sample quality, we have prepared several samples of LuPtBi with Bi-rich self-flux method as described in the above section. Temperature dependences of MR and carrier mobility of them have been measured and analyzed in our previous work of Ref. 8. As seen in Table 1[8], the residual resistivity ratio RRR and carrier mobility vary with samples. In the present work, we choose the sample S1 with the highest quality, that is with the largest RRR and highest carrier mobility (~79000 cm^2/Vs at 2K), to study the FS-related properties.

Half-Heusler LuPtBi crystallizes in a highly symmetric face-centered-cubic structure (see figure 1a). When seen from the highly symmetric [111] direction, as shown in figure 1b, it composes of alternate hexagonal and triangle atomic planes. Thus the single crystal LuPtBi usually takes a large hexagonal or triangle surface (figure 1d), which is indexed as (111) plane. The band structure and FS of LuPtBi were calculated using WIEN2k code (see Methods for details), and presented in figure S1 in the supplementary materials. The FS comprises eight needle-shaped electron pockets that orient in the highly symmetric Γ-L [111] direction and two near-spherical hole pockets centered around the Brillouin zone origin (the smaller one is encased by the larger one). Due to its compensated nature [8,28], the total volume of electron and

hole pockets are almost equal. Figure 1c shows the FS viewed from [111] direction, where the electron pockets exhibit six-fold symmetry and the hole pockets changed little with rotating. We note that the electron ellipsoid is rather anisotropic: the long axis is approximately three times longer than the short axis, which indicates the anisotropic nature of the effective mass. This rather simple and anisotropic structure of the FS provides opportunity to study the electronic structure of LuPtBi via angle-dependent magnetotransport properties. In similar anisotropic multi-valley systems, such as bismuth [14, 29] and $PdCoO_2$ [30], by rotating the single-crystalline samples to the magnetic field they obtained six-fold symmetric MR pattern, which proved to be closely correlated with the topology of the FS. One can use a simple classical picture to explain this phenomenon, whereby MR is dominated by the orbital effects originating from the cyclotron motion of electrons due to the Lorentz force. According to a standard two band model [31], MR can be scaled with $\mathrm{MR} \sim (w_c\tau)^2 \sim (e\tau/m^*)^2B^2 \sim \mu^2B^2$ (τ is the scattering time, m^* is the effective mass, and B is the magnetic field, $w_c(=eB/m^*)$ is the cyclotron frequency). Thus, the values of angular MR of metallic or semi-metallic systems, are strongly dependent on the anisotropy of the effective masses of carriers, which is directly related to the shape of the FS[5,10,14, 29].

To obtain the angle-dependent transverse MR, we applied the current I in the (111) plane, with four electric contacts in the [11-2] orientation (in the (111) plane [11-2] and [1-10] are two directions perpendicular to each other), as seen in figure 1e, and recorded the resistance when rotating the sample to the magnetic field. As a result, the six electron valleys detected are FS projected in the [11-2] direction, where two electron ellipsoids are not equivalent with the other four (figure 1f). It should be noted that the current direction kept perpendicular to the field ($B \perp I$) during the rotation. Unlike the longitudinal mode ($B \parallel I$), this geometry can substantially reduce the influence of the current path to MR in low-carrier density semi-metals[32, 33].

4. Angle-dependent magnetoresistance

4.1. For room temperature

Based on the above configuration ($B \perp I$), we measured the angular-dependent MR for a series of temperatures and magnetic fields. A typical set of data at T = 300 K is presented in figure 2a. A multi-peak fit is applied to resolve all peaks, as indicated by

the grey line under the B = 4T curve, and six distinguished peaks are independently identified with intervals very close to the location of the calculated electron ellipses (see figure 1f). When the magnetic field is parallel to the longer axis of the ellipses, MR is maximized because the carriers are traveling with smaller effective mass in this direction; thus an oscillating MR can be obtained by sweeping the magnetic field swept in a complete circle. Furthermore, two sizes of electron valley dictate that there are two peak heights. Next, a polar plot of the MR data (see figure 2b) reveals a near-perfect reproduction of the electronic FS shown in figure 1f, including the angles between adjacent peaks. Since hole conduction is less anisotropic, it can be taken as a squeezed sphere, contributing a nearly isotropic background. The magnetic-field-dependent resistivity $\rho(B)$ is normalized by $\rho_{\min}$ (the minimal value of the oscillating resistivity) in the polar plot, such that the radii reflect the strength of the anisotropy. At T = 300 K, the anisotropy reaches ~12% at B = 10 T, which is much larger than that (~1%) observed in other metals with simple spherical FSs [34]. But it should be noted that at smaller fields, for example B = 1-3T, the six peaks are not clearly resolved. As seen in the enlarged view in figure S2, it exhibits nearly only two peaks at B=1T. This is because the critical resolved fields can be varied with material types, depending on the effective mass anisotropy magnitude. In the highly anisotropic bismuth [14, 29], it may only need ~1T at room temperature (RT), while in LuPtBi, it is about 3-4T before the full details are revealed. Still, the pronounced oscillation of MR at RT is owing to the high carrier mobility exceeding 10^4 cm^2/Vs at RT in S1[8]. Moreover, we find that the symmetry of the MR pattern remains unchanged at a higher magnetic field of B~10T, it implies an invariant FS under strong magnetic-fields and at high-temperatures.

4.2. For various temperatures.

We fix the magnetic field B in two characteristic direction of [111] and [1-10], and obtain two sets of $R(T)$ curves (see figure 3a) by lowing the temperature under a series of constant magnetic fields. It can be seen that in both directions, the magnetic field largely enhances the resistance. When B is along the [111] direction, similar to the results in Ref. 8, the resistance changes monotonically in the entire temperature range. However, when measuring in [1-10] direction, under higher B the resistance firstly grows, then drops with approaching lower temperature. Hence, this anisotropic behavior indicates some alteration of the inner electronic structure.

To map out the transition in three dimensional space, we measured the angle dependence of MR by fixing the magnetic field at a lower value of B = 2 T and a higher value of B = 10 T. The original MR data and normalized $\rho(B)/\rho_{\min}$ are shown in figure 3b and figure S3, respectively. At B = 2 T, as temperature decreases, the average magnitude of MR first drops a bit and then increases to a higher value, in accordance with the $R(T)$ trend at B = 2 T presented in figure 3a. This trend is prevailed in all direction we studied, reflecting that the anisotropic symmetry remains unchanged throughout the entire temperature range under weak magnetic fields. However, at B = 10 T, despite the overall MR increases when reaching lower temperatures, at θ = 0° or 180°([1-10]), the growing-trend is violated. This indicates that the symmetry of the valleys was altered at low temperatures under strong magnetic fields. This assumption is further evidenced by comparing the normalized $\rho(B)/\rho_{\min}$, as shown in the insets. Under the weak magnetic fields, the polar plots of MR maintain a rough six-peak structure over the entire temperature range; however, plots indicate an unexpected transformation into a two-fold structure with decreasing temperatures, where two lobes in the θ = 0° or 180° ([1-10]) directions gradually vanished. Note that at T = 2 K and B=10 T, the transverse resistance of LuPtBi are oscillated with magnetic field due to the Landau quantization [8] and the semi-classical theory that connected the angle-dependent MR to the FS might not be applicable. Nevertheless, as discussed in Refs. 14 and 22 and according to our measurements (see figure S4), quantum oscillation is expected to only contribute a small modification to the large non-saturating MR background. Therefore, as we will see below, the observed unusual symmetry change in LuPtBi crystals under strong magnetic fields and low temperatures should be indicative of the rearrangements of the FSs.

To further investigate the correlation between the anisotropic behavior of MR and Fermi valleys in LuPtBi, we measured angle-dependent MR across a wide range of temperatures and magnetic fields. figure 4a shows normalized $\rho(B)$ in a polar plot obtained at T = 2K, between 0.5 and 12 T magnetic fields (MR data measured at other temperatures are presented in figure S4). Below 5 T, MR changes synchronously in all directions with increasing magnetic field over the entire temperature range up to 300 K, with no alteration in symmetry. However, when the strength of the magnetic field further increased, MR begins to change depending on directions: the magnitude of

MR increases along the [111] direction and decreases in the [1-10] direction, creating the final symmetrical transformation from a six-fold-like to a two-fold-like polar plot. The contour plot of the data in figure 4b is a more intuitive vision of the symmetrical transformation, showing that four blue-green islands transform into two red islands with increasing magnetic field. To obtain a continuous boundary of the symmetrical transformation, we plotted the magnetic field dependent $\rho(B)/\rho_{\min}$ along the [111] and [1-10] directions from 2 to 300 K (see figure 4c). Along the [111] direction, the $\rho(B)/\rho_{\min}$ value steadily increases for all magnetic field strengths and temperatures, but along the [1-10] direction, the curve begins to bend at a certain magnetic field strength and temperature, indicating the variation of anisotropy. The dotted red line marks the (*B*, *T*) boundary where the bend occurs. We can roughly define the critical transition magnetic field *B** as the intersection of the red line and the curve. It can be seen that the lower temperature, the smaller critical magnetic field needed, and that a change in symmetry can still be observed up to 100 K for $B > 10$ T. This qualitative description reveals the trend similar to the results in the well-studied bismuth semimetal [29], where complex quantitative calculations based on a tensor mobility model were performed. To eliminate the effects of geometry and/or possible imperfections of the single-crystalline samples on the observed loss of six-fold symmetry, we also investigated another high-mobility sample S3. As shown in supplementary figure S5, very similar angled-dependent MR behaviors were obtained, indicating that the origin of the change in the FSs is intrinsic.

5. Quantum oscillations and Fermi-surface topology at high-fields.

We now turn our attention to the electronic structure at high-fields. The loss of six-fold symmetry on the topology of FS in LuPtBi suggests that electron pockets are altered and, consequently caused the sign reversal of Hall resistivity and thermopower at high-fields. As aforementioned and previously reported in our work in Ref. 8, in the low-temperatures and high-fields region, quantum transport arises in LuPtBi because of the small effective mass and high carrier mobility. It is worth noting that the angular-dependent of Shubnikov-de Haas (SdH) quantum oscillations have been taken as a powerful tool to probe the FSs[2,10,35-36]. Hence, in order to explore the topology of FSs under high-fields, we have measured the angular-dependent of SdH oscillations at $T = 2$ K between 0° (in the [1-10] direction) and 90° (in the [111]

direction) by rotating the sample while maintaining the magnetic field perpendicular to current ($B \perp I$) up to 13 T. The original $R(B)$ curves are shown in the supplementary figure S6. To clearly present quantum oscillations, we plotted the second derivative of resistance with respect to magnetic field, $\mathrm{d}^2R/\mathrm{d}B^2$ as a function of $1/B$ in figure 5a. Periodic oscillations are evident in all directions with slightly varied periods, indicating a slightly anisotropic 3D FS shape at high-fields.

To inspect the high-field FS, we performed corresponding fast Fourier transform (FFT) analysis to the SdH data. As shown in supplementary figure S7, when we performed FFT analysis over a broad range of magnetic fields (~ 8-13T), there are several peaks observed, which is consistent with our previous temperature-dependent SdH analysis (see Ref. 8). The lower peak is corresponding to the electron, while the main peak should belong to the hole, owing to the difference in the effective masses (also see discussions in Ref. 8). But when inspecting a higher field range of 10-13T, as shown in figure 5b, there only leaves the peak around 200 T that should correspond to the hole. We will further confirm this from the analysis of anisotropy and effective masses.

The largest cross section of the FS is linearly proportioned to the frequency according to the Onsager relation of $S_F = \frac{2\pi e}{\hbar} F(\theta)$, where e is the electron charge and $\hbar$ is the Planck constant divided by 2π. From the FFT frequency spectrum in figure 5c, it is apparent that the cross-sectional area of the FS is maximized at $\theta \sim 0°$ (the magnetic field is along the [1-10] direction) and decreases to a minimum at $\theta \sim 60°$ with increasing angle size, after which it then increases again up to 90°(the magnetic field is along the [111] direction). The behavior of this angle-dependent FS is distinguished from that in systems with a single-elliptical FS[35], where the behavior can be described by $F(\theta) \sim \cos 2\theta$ and the magnitude continually changes from 0° to 90°. Meanwhile, the anisotropy of the amplitude remains comparatively low ($S_{\max}/S_{\min} \sim 1.22$), which suggests that the overall anisotropy of the FS is much weaker than that observed in the weak-magnetic-fields and high-temperatures regime. Hence, it should not correspond to the electron pockets, which are elliptical and high anisotropic. By following the cross-section change of that represented by the frequency spectrum, we draw a sketch of the represented FS (figure 5d). It is near-spherical with squeezed valleys at $\theta \sim 60°$ due to the frequency dip around this angle. This sketch is resembling to the theoretical hole Fermi pockets as depicted in

figure 1f.

The anisotropic FS can be also described by the effective mass, which can be extracted from the temperature dependence of the amplitudes of the SdH oscillations. According to the standard Lifshitz-Kosevich theory, the cyclotron effective mass of the carriers (m_e) can be obtained by fitting the temperature dependence of the SdH oscillation amplitudes with a thermal damping factor, $\Delta R_T \propto \frac{2\pi^2 k_B T/\hbar w_c}{\sinh[2\pi^2 k_B T/\hbar w_c]}$ where k_B is Boltzmann's constant, T is temperature and $w_c = eB/m^*$ is the cyclotron frequency. Figure 5e shows the data for θ = 0° and 60°, the two extremes corresponding to the maximum and minimum effective masses, respectively. The fitted effective masses are 0.24 m_e and 0.3 m_e (m_e is the free electron mass) for θ = 60° and θ = 0°, respectively, which correspond to the hole carriers, also consistent with results in Ref.8. The low anisotropy of the effective masses again suggests the reduced anisotropy of the FS at low-temperatures and under high-fields. Thus the SdH evidences of a high-field hole-like conduction, in combination with the symmetry change in the angular MR, suggest that some kind of FS transformation, like the electron-hole transition may take place.

6. Discussion and summary

Hereto we have observed a transformation of the angular MR from having a highly anisotropic six-fold valley to a slightly anisotropic two-fold valley at low-temperatures (< 10 K) and under high-fields. As the angular MR is closely related to the electron FS of LuPtBi in our case, the symmetry and anisotropy change in the angular MR suggest some changes in the FS. Meanwhile, the angular SdH oscillations indicate vanishing of high-anisotropic electron conduction, also implying a magnetic-field induced electronic structure change. Field-induced FS reconstruction has also been reported in several specific systems[25,26,35-38], but the physics behind the phenomena remains a wide-open question. In fact, it has been reported that a strong magnetic field can rearrange the energy spectrum by displacing band edges by quantization, where the conduction band edge shift upwards and the valence band downwards, thus creating a band-gap in gapless semiconductors[39]. In the picture of ours, the high-mobility electrons with small effective mass dominate and induce the negative Hall resistivity at low fields[8]. When the quantization of the high-mobility electron carriers occur, the concentration of electrons and holes are changed in order

to keep the Landau levels filled. As the electrons and holes are both in a small amount, a field-induced Lifshitz transition can be accompanied. The abnormal sign reversal of Hall resistivity and thermopower in LuPtBi at high magnetic fields [8] can be understood in terms of this transition. The field-induced FS reconstruction can be taken as an origin for the appearance of large positive MR in the compensated semimetal LuPtBi, like in the case of $NbSb_2$[3].

To conclude, using measurements of the angular-dependent transverse MR and SdH quantum oscillations, we have successfully mapped out the FS topology of LuPtBi, and furthermore, indentified an unexpectedly field-induced FS change at low-temperatures. Further theoretical studies and experiments should help clarify how the electron evacuation and FS reconstruction takes places in LuPtBi. Nevertheless, we expect that the strategy of FS reconstruction would provide useful guidelines for the development of giant MR effect as high-performance magnetoresistive devices in other known compensated semimetals and open an area of research of both fundamental and applied importance.

References

1. Yang F Y, Liu K, Hong K, Reich D H, Searson P C and Chien C L 1999 *Science* **284** 1335-1336.
2. Ali M N *et al* 2014 *Nature* **514** 205.
3. Wang K F, Graf D, Li L, Wang L and Petrovic C 2014 *Sci. Rep.* **4** 7328 .
4. Yang F Y, Liu K, Hong K, Reich D H, Searson P C, Chien C L, Wang Y L, Zhang K Y and Han K 2000 *Phys. Rev. B* **61** 6631-6636.
5. Zhao Y F *et al* 2015 *Phys. Rev. B* **92** 041104(R)
6. Shekhar C, Ouardi S, Nayak A K, Fecher G H, Schnelle W and Felser C 2012 *Phys. Rev. B* **86** 155314.
7. Wang W H, Du Y, Xu G Z, Zhang X M, Liu E K, Liu Z Y, Shi Y G, Chen J L, Wu G H and Zhang X X 2013 *Sci. Rep.* **3** 2181.
8. Hou Z P *et al* 2015 *Phys. Rev. B* **92** 235134 .
9. Shekhar, C, Kampert E, Foerster T, Yan B H, Nayak A K, Nicklas M, Felser C *arXiv:*1502.00604.
10. Zhao Y F *et al. Phys. Rev. X* **5** 031037 (2015).

11. Wang H, Wang H C, Liu H W, Lu H, Yang W H, Jia S, Liu X J, Xie X C, Wei J and Wang J 2016 *Nat. Mater.* **15** 38-42.
12. Neupane M *et al* 2014 *Nat. Commun.* **5** 3786.
13. Liu Z K *et al.* 2014 *Science* **343** 864 -867.
14. Zhu Z W, Collaudin A, Fauqué B, Kang W and Behnia K 2012 *Nat. Phys.* **8** 89-94 .
15. Kang D F *et al* 2015 *Nat. Commun.* **6** 7804.
16. Pan X C *et al.* 2015 *Nat. Commun.* **6** 7805.
17. Xiao D, Yao Y G, Feng W, Wen J, Zhu W, Chen X Q, Stocks G M, Zhang Z Y. 2010 *Phys. Rev. Lett.* **105** 096404 .
18. Chadov S, Qi X L, Küler J, Fecher G H, Felser C, Zhang S C. 2010 *Nat. Mater.* **9** 541-545.
19. Lin H, Wray L A, Xia Y Q, Xu S Y, Jia S, Cava R J, Bansil A and ZHasan M 2010 *Nat. Mater.* **9** 546-549.
20. Zhang X M, Hou Z P, Wang Y, Xu G H, Shi C L, Liu E K, Xi X K, Wang W H, Wu G H and Zhang X X 2016 *Sci. Rep.* **6** 23172 .
21. Xu G Z, Wang W H, Zhang X M, Du Y, Liu E K , Wang S G, Wu G H, Liu Z Y, Zhang X X 2014 *Sci. Rep.* **4**, 5709 .
22. Liu, C. *et al.* 2011 *Phys. Rev. B* **83**, 205133.
23. Liu, Z. K. *et al.* 2016 *Nat. Commun.* **7**, 12924.
24. Lifshitz I M 1960 *Zh. Eksp. Teor. Fiz.* **38** 1569.
25. Rosenbaum T F, Field S B, Nelson D A and Littlewood P B1985 *Phys. Rev. Lett.* **54** 241-244.
26. Kozlova N *et al.* 2005 *Phys. Rev. Lett.* **95**, 086403.
27. Kokalj A 2003 *Comp. Mater. Sci.* **28** 155. Code available from http://www.xcrysden.org/.
28. Sawai W A, Lin H, Markiewicz R S, Wray L A, Xia Y, Xu S Y, Hasan M Z and Bansil A 2010 *Phys. Rev. B* **82** 125208.
29. Collaudin A, Fauque B, Fuseya Y, Kang W and Behnia K 2015 *Phys. Rev. X* **5** 021022 .
30. Takatsu H, Ishikawa J J, Yonezawa S, Yoshino H, Shishidou T, Oguchi T, Murata K, and Maeno Y 2013 *Phys. Rev. Lett.* **111**, 056601.
31. Abrikosov A A 1988 *Fundamentals of the Theory of Metals* (North-Holland, Amsterdam).

32. Yoshida K 1975 *J. Phys. Soc. Jpn.* **39** 1473–1481 .
33. Arnold F *et al* 2016 *Nat. Commun.* 7 11615.
34. Overhauser A 2011 *Anomalous Effects in Simple Metals*. (Wiley-VCH Berlag GmbH & Co. KGaA,Weinheim).
35. Xiang F X, Wang X L, Veldhorst M, Dou S X and Fuhrer M S 2015 *Phys. Rev. B* **92** 035123 .
36. Thoutam L R, Wang Y L, Xiao Z L, Das S, Mayer A L, Divan R, Crabtree G W, and Kwok W K 2015 *Phys. Rev. Lett*. **115** 046602.
37. Sebastian S E, Harrison N, Mielke C H, Liang R X, Bonn D A, Hardy W N, Lonzarich G G 2009 *Phys. Rev. Lett*. **103** 256405.
38. Pletikosić I, Ali M N, Fedorov A V, Cava R J and Valla T 2014 *Phys. Rev. Lett*. **113** 216601.
39. Tsidilkovski I M 1997 *Electron Spectrum of Gapless Semiconductors*. Springer-Verlag Berlin Heidelberg.

Acknowledgements

This publication is based upon work supported by the King Abdullah University of Science and Technology (KAUST) Office of Sponsored Research (OSR) under Award No: CRF-2015-2549-CRG4, National Natural Science Foundation of China (Grant Nos. 51571121 and 11604148), Jiangsu Natural Science Foundation for Distinguished Young Scholars (Grant No. BK20140035), Natural Science Foundation of Jiangsu Province (Grant No. BK20160829) and Qing Lan Project of Jiangsu Province. It is also funded by the Priority Academic Program Development of Jiangsu Higher Education Institutions.

Sample	RRR ρ_{300K}/ρ_{2K}	MR 2K, 10T	μ_e $cm^2V^{-1}s^{-1}$	μ_h $cm^2V^{-1}s^{-1}$
S1	4.3	3200%	79000	7320
S3	4.1	3000%	74000	5400
S5	3.4	1900%	31000	5000
S6	2.6	1000%	12000	4300
S9	2.3	353%	8200	2500
S12	1.4	136%	-	2400

Table 1. Magnetotransport parameters for different samples that we have prepared, taken from the supplemental materials of Ref. 8. RRR represents the ratio of $\rho_{xx}(300\text{K})/\rho_{xx}(2\text{K})$. The mobility μ_e and μ_h of S1, S3, S5, S6, S9 and S12 were obtained with two-carrier model fit of MR and Hall data of these samples (adapted from ref. 8).

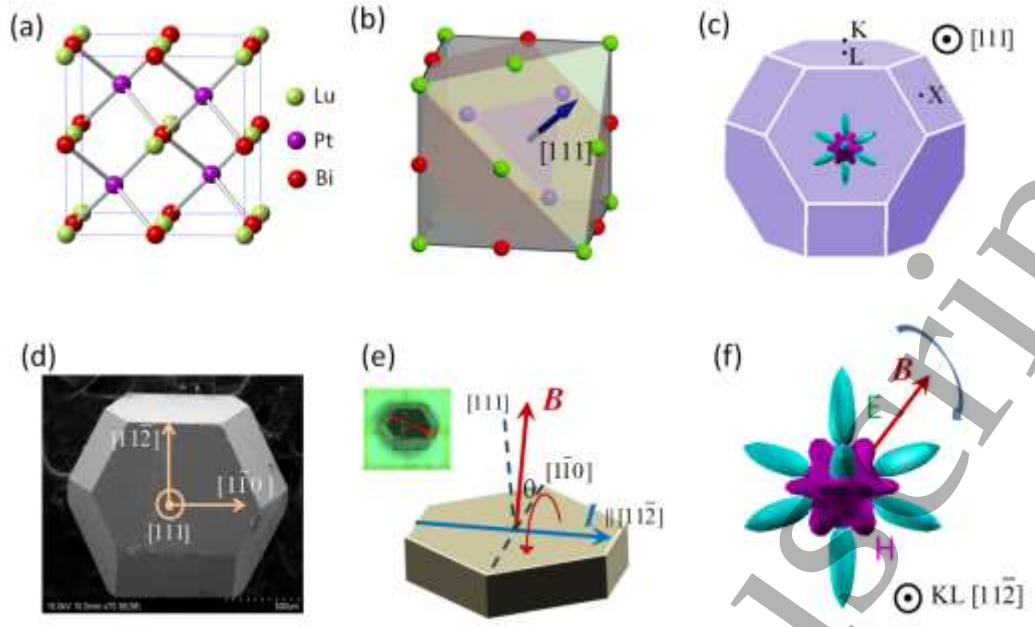

Figure 1. (a) Face-centered cubic structure of half-Heusler LuPtBi, with space group of $F\bar{4}3m(216)$. (b) 3D structural model of the lattice revealing the cleavage (111) plane. (c) Calculated FS seen in the direction of Γ-L [111] in the first Brillouin zone: the cyan pockets belong to the electrons and the pink one represent the hole. (d) A typical scanning electron microscopy image of LuPtBi single crystal. The hexagonal surface is (111) plane, the two directions perpendicular to [111] direction are defined as [11-2] and [1-10], respectively. (e) Schematic of the experimental configuration used to record the angular-dependent MR. The constant current *I* was applied along [11-2] direction, while the magnetic field *B* was rotating in the (111, 1-10) plane. The two vectors *B* and *I* were kept normal to each other during the rotation. Inset is the real crystal we used, with the red arrow indicating the current direction. (f) FS projected in the direction K-L [11-2], where the electron ellipses are not all equivalent , and the hole is like a distorted sphere.

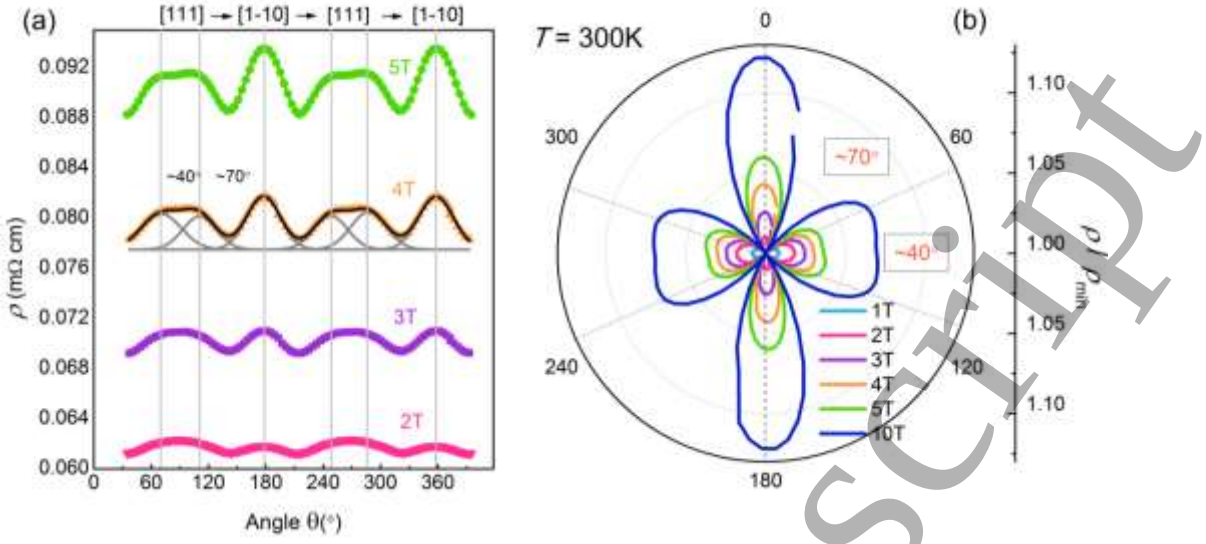

Figure 2. (a) Angular dependence of MR by rotating the sample from 0° to 360° measured at 300K. The multi-peak fit under the 4 T curve (grey line) shows six resolved peaks positioned in consistent with the distribution of electron Fermi pockets shown in Fig. 1f. (b) Polar plots of the normalized MR data at different magnetic fields.

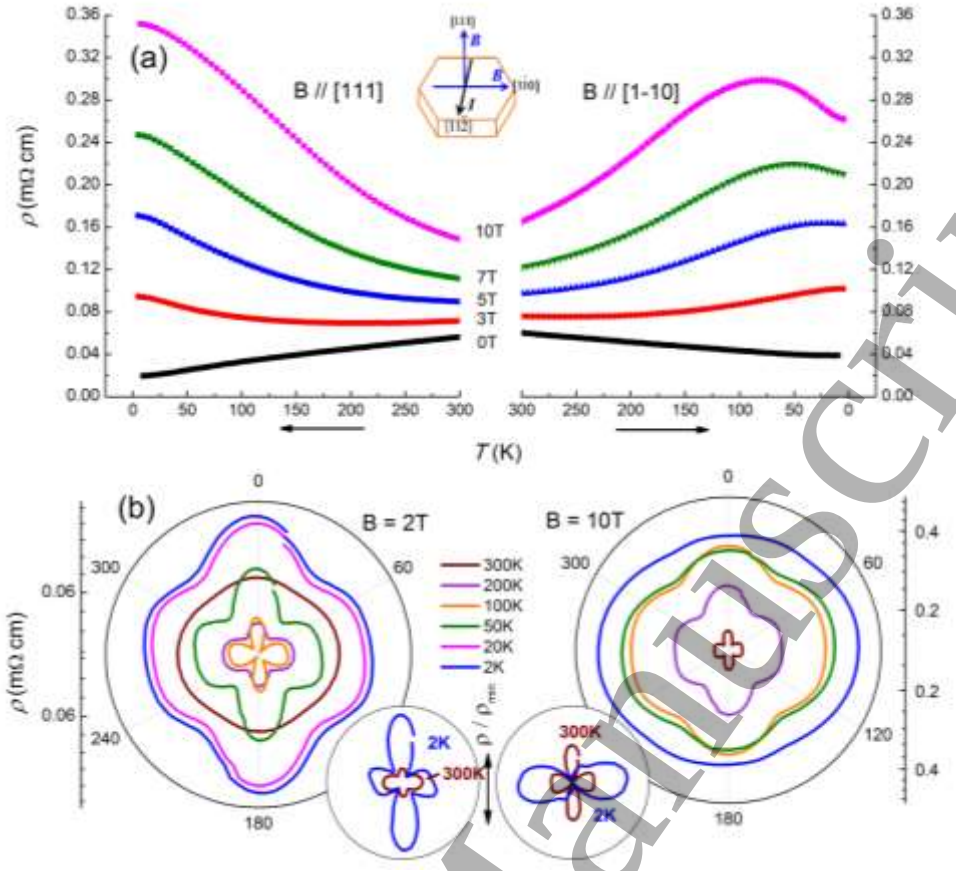

Figure 3. (a) Resistance as a function of temperature for different magnetic fields along the [111] and [1-10] directions, respectively. (b) Polar plots of angular dependence of MR at two fixed fields (B=2 and 10 T) for different temperatures. Insets show the normalized resistivity ($\rho/\rho_{\min}$) at T = 2 and 300 K, respectively.

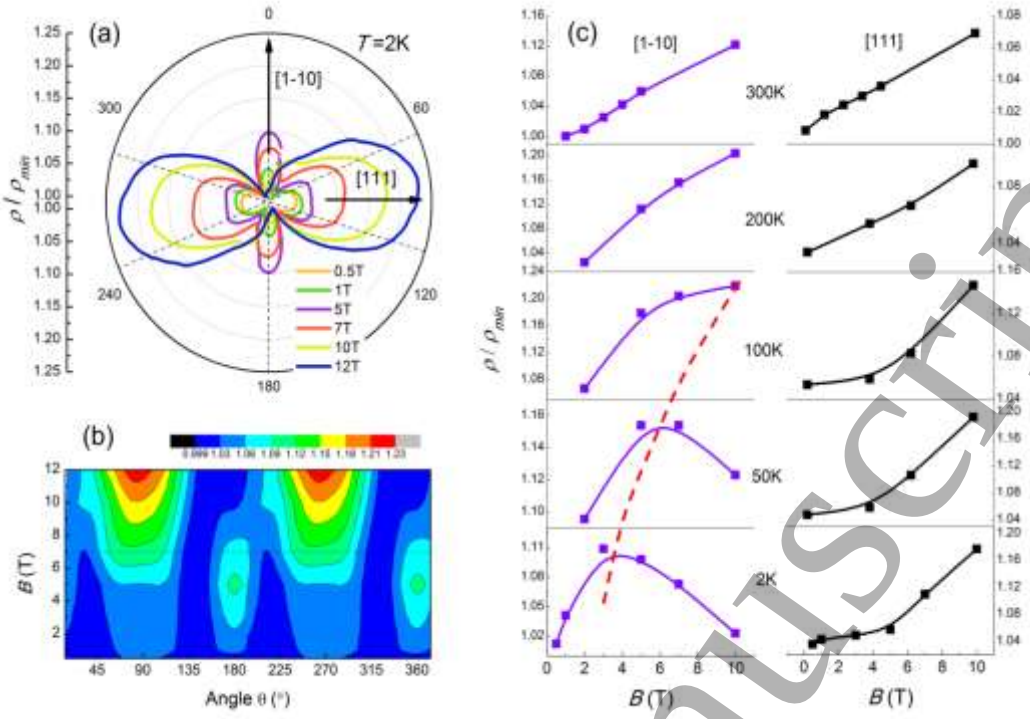

Figure 4. (a) Polar plots of angle dependence of normalized magnetoresistivity $\rho(B)/\rho_{\min}$ at T = 2 K from 0.5 T to 12 T. The [111] and [1-10] direction point towards θ = 90° and θ = 0°, respectively, as denoted in Figure 1. (b) Contour plot of data in (a), where color represents the normalized magnitude of MR. (c) Magnetic-field dependence of $\rho(B)/\rho_{\min}$ in [111] and [1-10] directions at different temperatures. The dotted red line marks the magnetic field-temperature, where the curve begins to bend.

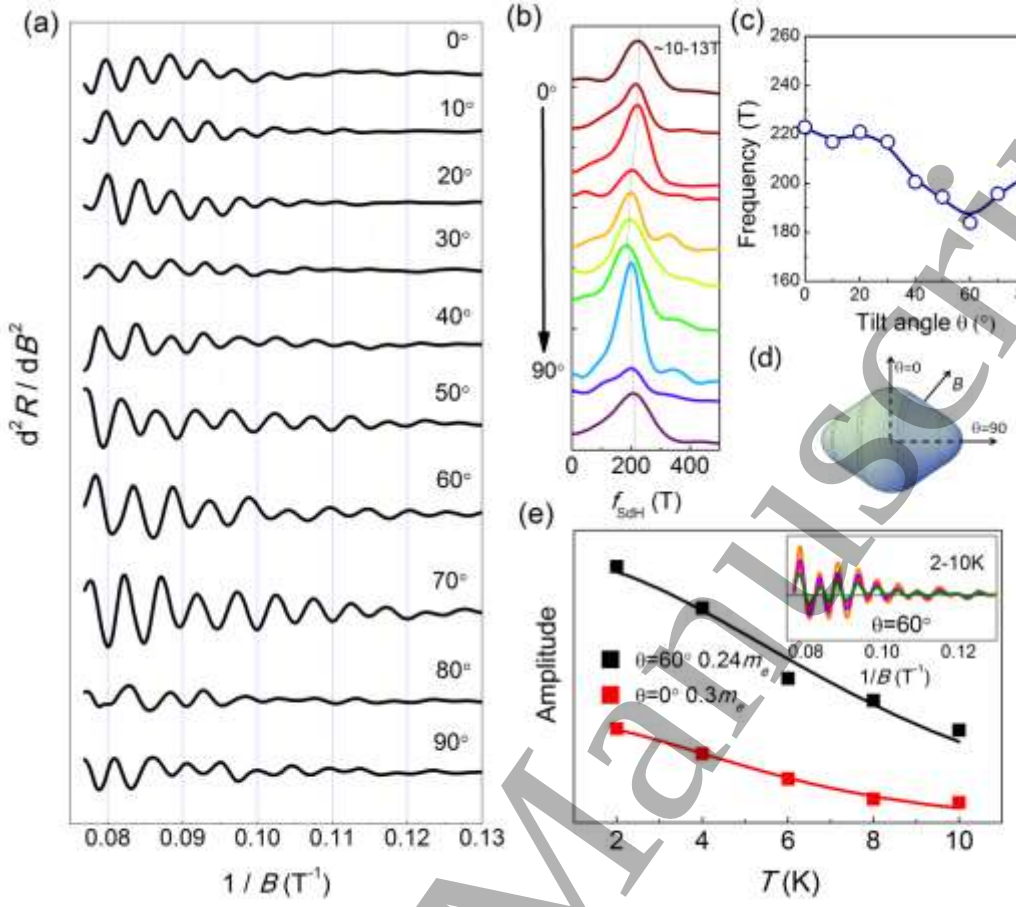

Figure 5. (a) The second derivative of MR, d^2R/dB^2, as a function of $1/B$ at 2K between θ = 0° ([1-10] direction) and 90° ([111] direction). (b) FFT spectra of data in (a) under the magnetic field ranges of 10-13T. (c) Angle dependent of the oscillation frequency. (d) A sketch of a 3D ellipsoid hole Fermi pocket deduced from the frequency spectrum in (c). (e) Temperature dependences of the oscillation amplitude for θ = 60° (black squares) and θ = 0° (red squares) and their fitting to the Lifshitz-Kosevich formula (solid lines), as explained in the main text. The inset is the oscillatory part of R versus $1/B$ for different temperatures at θ = 60°.